

## A Secondary Flow Model for the Planetary Boundary Layer<sup>1</sup>

R. A. BROWN

*Dept. of Atmospheric Sciences, University of Washington, Seattle*

(Manuscript received 8 December 1969, in revised form 8 May 1970)

### ABSTRACT

The equations of motion for a neutrally buoyant fluid are solved to produce an equilibrium flow consisting of a modified Ekman spiral mean flow plus a helical secondary flow. By considering the secondary flow to be a finite perturbation on a mean large-scale flow, approximate equations are obtained for the secondary flow and the modified mean flow as functions of the large-scale parameters. When the energetics of this system are considered, an equilibrium magnitude for the secondary flow can be obtained.

The finite perturbations are assumed to preserve the structure of the infinitesimal perturbation solutions for the dynamic instability of the Ekman boundary layer. In particular, helical rolls occur as finite perturbation solutions. These finite disturbances are found to alter the mean Ekman velocity profile such that it becomes stable. The rolls, with characteristic depths of 5–7 times the Ekman characteristic length and corresponding wavelengths of  $4\pi$  times this parameter, may be frequent occurrences in both atmospheric and oceanic boundary layers.

### 1. Introduction

There exists at present a need for a planetary boundary layer model to complement the relatively successful synoptic-scale, or “free-stream” models. Most of the effort in planetary boundary layer theory has been directed toward developing the microscale analysis, hoping that it can subsequently be generalized to include mesoscale boundary layers. There has been a relative lack of interest, or progress, in the understanding of large-scale boundary layer dynamics. This has been partially due to the complexity of the governing equations which must include the rotation terms—and hence three-dimensionality. Perhaps the most serious setback to the successful large-scale geophysical boundary layer analysis lies in the failure of the elementary equilibrium balance between pressure, viscous and Coriolis forces, first solved by Ekman (1905), to be verified observationally, especially in the atmosphere. The assumption of a “virtual coefficient of friction” has been generally taken as the flaw in this theory, and attention has been directed to the turbulent nature of the flow, from whence this term arises. However, from a practical standpoint, it is desirable to parameterize the flow near the boundary with respect to a single

characteristic quantity which describes the nature of the boundary, i.e., its roughness. Thus, the intention in this paper is to synthesize a boundary layer model based on some of the theoretical facts and observations, and which relates the flow field to a parameter representing the mesoscale boundary condition.

Recently, the observed existence of well-ordered mesoscale flows within the planetary boundary layer has suggested that a non-random, laminar-like theory may be appropriate to this region. One of the first discussions of atmospheric band structure was given by Kuettner (1959). His work includes many observations of parallel cloud lines, which he has related to helical motion in the boundary layer (Kuettner, 1967). In an interesting study, Woodcock (1942) observed that the flight pattern of soaring gulls indicated the presence of line updrafts under certain conditions. Kuettner (1959) discussed glider pilot's experiences in long (500 km) lifting bands at heights up to 2–3 km. The most obvious and frequent indication of secondary motions comes from satellite photos. A particularly good example is shown in Fig. 1a, the pertinent meteorological information being given in Fig. 1b. Numerous photos of cloud streets can be found in Plank (1965) and NASA (1967). In addition, evidence of rows of helical motions have appeared on radar observations (Hicks and Angell, 1968) and tetron observations (Angell *et al.*, 1967, 1968). The latter resulted from the first experiments

<sup>1</sup> Contribution No. 223, Department of Atmospheric Sciences, University of Washington, Seattle.

devised specifically to measure the ubiquitous rolls in the atmosphere.

Other geophysical occurrences of secondary roll flows have been discussed by Langmuir (1938) in his notes and observations on Lake George. He observed and roughly measured helical circulations near the surface which correspond to the secondary flows developed in the model derived herein. Rolls provide a possible explanation for the long streaks common to the ocean's surface (Faller, 1965; Roll, 1965, p. 119). Hanna (1969) has suggested planetary boundary layer rolls as the cause of the long, parallel alignment of sand dunes in large deserts (see NASA, 1967).

This paper attempts to explain these phenomena with a planetary boundary layer model. The method used here establishes the secondary flow as an equilibrium perturbation. The flow is separated into the primary (or mean) flow, and the secondary (or zero mean finite perturbation) flow. The lateral and vertical structure of the disturbance, as determined by the lateral wavelength and the vertical amplitude and phase relations, is assumed to be determined by the most unstable infinitesimal perturbation from the solution to the first-order stability equation. The modified mean flow is then calculated as a function of the normalized disturbance amplitude using the mean flow equations including the Reynolds stress terms. The equilibrium amplitude is determined from an equilibrium energy balance. This finite perturbation procedure has been successfully used by Stuart (1958, 1960) in the analysis of Poiseuille flow and the explanation of Taylor-Görtler vortices. Charney (1958) has employed this concept in his analysis of the general circulation zonal flow. Finite-amplitude perturbations were also considered by Malkus and Veronis (1958) in their convection studies.

## 2. Development of the general equations

### a. Basic equations

Since our concern is with the secondary flow, it would seem expedient to select a simple, basic, equilibrium flow, such as the Ekman boundary solution. However, since the governing equations are contingent upon the mean flow, the character of the basic mean flow equations shall first be investigated.

The basic set of nondimensionalized equations is comprised of the equations of motion for a viscous, compressible, rotational fluid, the first law of thermodynamics, and the equation of continuity. The concept of a "turbulent eddy viscosity" has been used in this model. Caution must be exercised when attempting an

analog between the turbulent stress-strain relation and the molecular Newtonian relation in order to achieve closure. The caution is warranted, in consideration of the much smaller gap in characteristic scales between the turbulent diffusion and the boundary layer characteristic dimensions, compared to the large gap associated with the scale difference between molecular motion and boundary layer motion. If a sufficient scale difference is present, then it is assumed that there exists a meaningful derivative limit for the mean flow without regard to the random character of the diffusive action of the small-scale turbulence. It must be admitted that in the atmospheric boundary layer, this is sometimes a tenuous assumption. However, observations clearly indicate laminar, or well-ordered, motions are frequent in planetary boundary layers. In this model the well-ordered small-scale phenomena are analyzed by laminar theory, and the assumption is made that the effect of the small-scale turbulence can be adequately parameterized in the same fashion that molecular stress effects have been handled with frequent success, e.g., in the Stokes' stress-rate of strain constituency relation.

In addition, the turbulent diffusivity coefficient (or Austausch coefficient)  $K_m$  is assumed to be constant. This assumption is also tied to the size distribution of the small-scale turbulent eddies, which are known to vary through the boundary layer in proportion to distance from the surface. However, this variation does not appear to be of essential importance to this analysis, and an integrated mean coefficient is used. It is noteworthy that the principles in this model require only that the ratio of characteristic turbulence dimension to boundary layer depth be small, so that there exists a mean flow. The presence of an inflection point in the lateral velocity profile is the only requirement for the dynamic instability, regardless of the model which develops this mean profile. Any new theory producing a lateral flow velocity profile can be easily substituted for the Ekman profile; thus, the analysis could be applied to a situation in which the thermal wind exhibits an inflection in the lateral velocity. The primary effect of eddy viscosity is to produce the mean profile shape in the Ekman boundary flow. Similarly, a constant coefficient  $K_h$  is assumed in the heat diffusion term. The basic set of equations is thus

$$\left. \begin{aligned} \dot{\mathbf{V}} + 2\boldsymbol{\Omega} \times \mathbf{V} + \nabla p / \rho + g\hat{\mathbf{k}} - K_m \nabla^2 \mathbf{V} &= 0 \\ \dot{\rho} + \rho \nabla \cdot \mathbf{V} &= 0 \\ \dot{T} + [p / (\rho c)] \nabla \cdot \mathbf{V} - K_h \nabla^2 T &= 0 \\ P &= \rho RT \end{aligned} \right\} \quad (1)$$

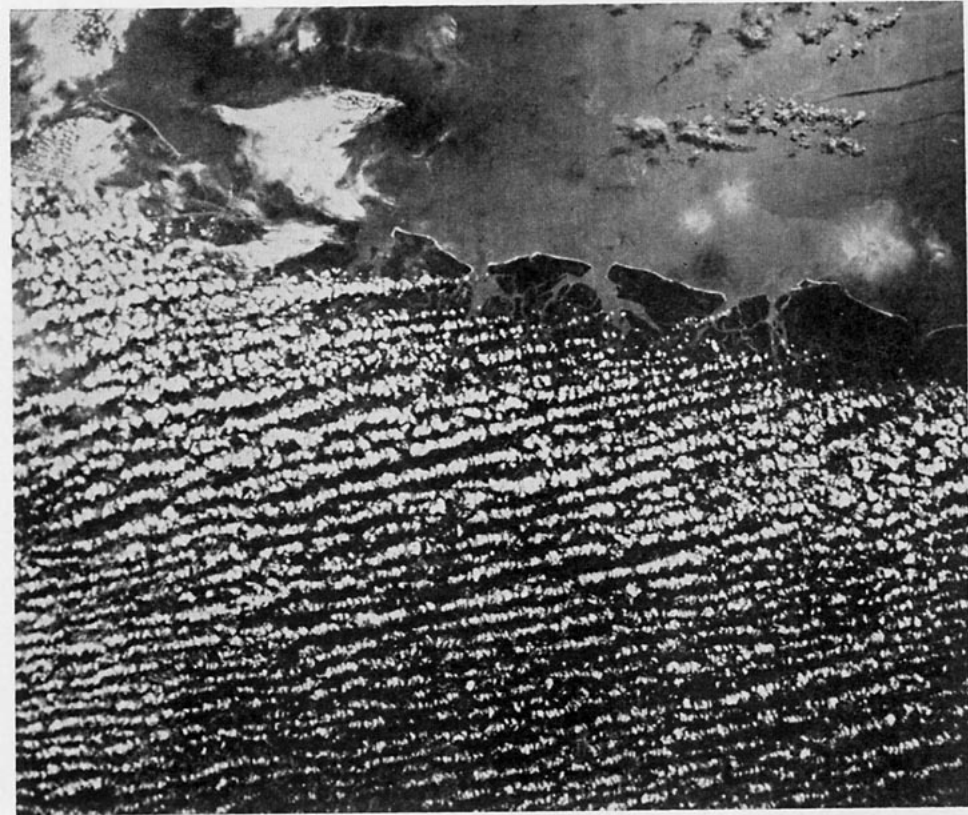


FIG. 1a. Apollo photo of the Georgia Coast at 1500GMT (1000 local time) on 4 April 1968, from a height of 125 mi. The cloud streets are over the land, aligned approximately with the geostrophic wind which is due north. They begin about 16 km after landfall, and occupy an area  $\sim 200$  mi<sup>2</sup>. The rows are about 2-3 km apart at about 1 km height. (The original photograph was in color).

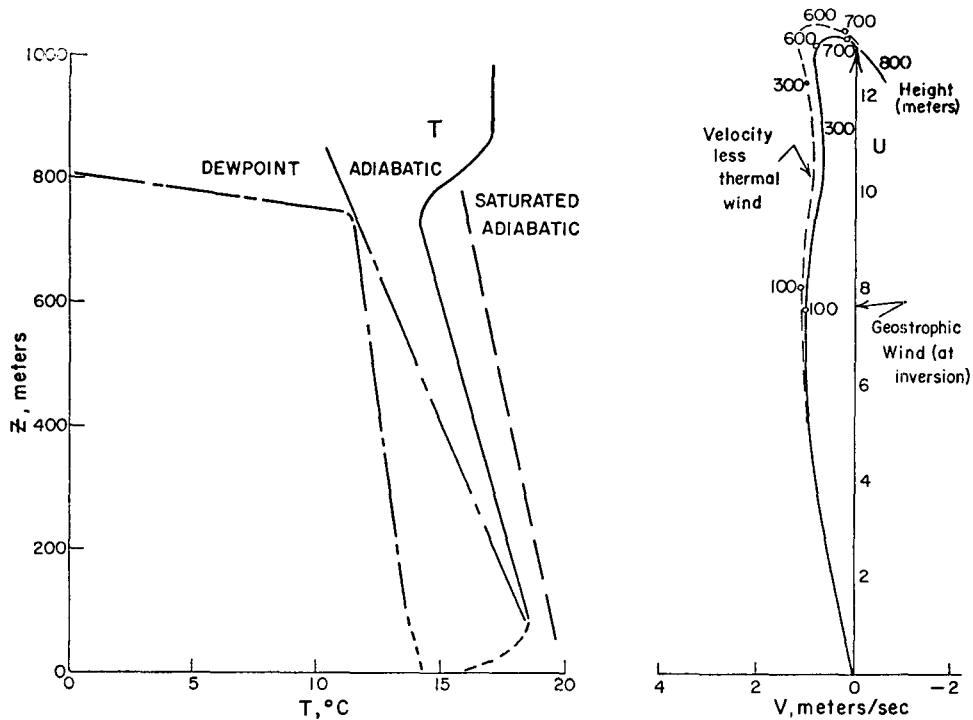


FIG. 1b. Radiosonde temperature, dew-point and velocity profiles for Jacksonville at 1200 GMT 4 April 1968.

Consider the steady-state flow. In the atmosphere, observations indicate that generally  $W \ll U$  or  $V$ . Also, satellite photos, such as Fig. 1a, indicate the existence of organized two-dimensional secondary flows approximately aligned parallel to the geostrophic flow. Hence, the velocity is separated into a horizontally homogeneous mean value plus a periodic perturbation with magnitude independent of the longitudinal coordinate. When this substitution is made, and the horizontal average is taken, the equations for the mean flow are

$$\left. \begin{aligned} f\bar{V} + K_m \bar{U}_{zz} - (\bar{v}u_y + \bar{w}u_z) - \bar{P}_x/\bar{\rho} &= 0 \\ f\bar{U} - K_m \bar{V}_{zz} + (\bar{v}v_y + \bar{w}v_z) + \bar{P}_y/\bar{\rho} &= 0 \\ (\bar{v}v_y + \bar{w}v_z) + g + \bar{P}_z/\bar{\rho} &= 0 \\ \bar{U}T_x + \bar{V}T_y - (\bar{v}T_y + \bar{w}T_z) - K_H \nabla^2 \bar{T} &= 0 \\ \bar{U}\bar{\rho}_x + \bar{V}\bar{\rho}_y &= 0 \end{aligned} \right\} \quad (2)$$

where a bar denotes a mean value.

*b. The Ekman/geostrophic mean flow*

In the unperturbed, or infinitesimal perturbation case, the equations governing the flow are

$$\left. \begin{aligned} f\bar{V} + K_m \bar{U}_{zz} - \bar{P}_x/\bar{\rho} &= 0 \\ f\bar{U} - K_m \bar{V}_{zz} + \bar{P}_y/\bar{\rho} &= 0 \\ g + \bar{P}_z/\bar{\rho} &= 0 \\ \bar{U}T_x + \bar{V}T_y + K_H \nabla^2 \bar{T} &= 0 \\ \bar{U}\bar{\rho}_x + \bar{V}\bar{\rho}_y &= 0 \end{aligned} \right\} \quad (3)$$

In the outer region, away from the wall's influence, the geostrophic equations successfully describe the flow. However, a uniformly valid solution for the entire region requires a boundary layer type solution to accommodate the wall effect—manifested in the no-slip boundary condition. The solution is simply a superposition of the familiar Ekman spiral plus a thermal wind. The solution, uniformly valid in  $0 \leq z \leq H$ , is

$$\left. \begin{aligned} f\bar{U} &= -\bar{P}_y/\rho + \exp[-z/\delta] \\ &\quad \times [\bar{P}_{0y} \cos(z/\delta) + \bar{P}_{0z} \sin(z/\delta)] \\ f\bar{V} &= \bar{P}_x/\rho + \exp[-z/\delta] \\ &\quad \times [\bar{P}_{0y} \sin(z/\delta) - \bar{P}_{0z} \cos(z/\delta)] \\ \delta &= (2K_m/f)^{1/2} \end{aligned} \right\} \quad (4)$$

The boundary layer thickness can be estimated at  $e^{-z/\delta} \ll 1$ . A good estimate results from  $z = \delta$ . With this hindsight, we may use  $\delta$  for the characteristic height appropriate to the  $U_{zz}$  term in the nondimensionaliza-

tion of (3). The velocity profiles are self-similar with respect to  $\delta$ . In the general case, all thermodynamic variables may be functions of  $x, y$  and  $z$ .

*c. Development of the approximate equations for secondary flow*

When the mean flow equations (2) are subtracted out of the complete exact perturbed equations, the disturbance equations remain, i.e.,

$$\left. \begin{aligned} \bar{V}u_y + w\bar{U}_z - fv - K_m \nabla^2 u + (vu_y + wu_z) \\ \quad - (\bar{v}u_y + \bar{w}u_z) &= 0 \\ \bar{V}v_y + w\bar{V}_z + fu - K_m \nabla^2 v + (vv_y + wv_z) \\ \quad - (\bar{v}v_y + \bar{w}v_z) + p_y/\rho - (\bar{P}_y/\bar{\rho})^2 \rho &= 0 \\ \bar{V}w_y - K_m \nabla^2 w + (vw_y + ww_z) \\ \quad - (\bar{v}w_y + \bar{w}w_z) + p_z/\rho - (\bar{P}_z/\bar{\rho})^2 \rho &= 0 \\ \bar{V}T_y + v\bar{T}_y + w(\bar{T}_z + g/c_p) + (vT_y + wT_z) \\ \quad - (\bar{v}T_y + \bar{w}T_z) - K_H \nabla^2 T &= 0 \\ p &= \rho\bar{T} + \bar{\rho}T \\ v_y + w_z &= 0 \end{aligned} \right\} \quad (5)$$

This is a complete set of six equations in the perturbation quantities  $u, v, w, p, T$  and  $\rho$ . However, with the large number of terms, they are not amenable to solution without simplification. In the absence of measured values of the secondary flow magnitudes, a systematic nondimensionalization of the equations is employed, resulting in equations which display, as coefficients, the important parameters of the flow. When the characteristic values used in the nondimensionalization have been carefully chosen, the effect of a variation of these parameters on the form of the solutions to the resulting equations can be investigated.

In this case, there are at least two characteristic scales, appropriate to the mean and secondary flows. The resulting dimensionless parameters will therefore involve combinations of these scales (e.g.,  $\Delta p_0/\Delta \bar{P}_{0H}$ ). Depending upon these ratios, various terms will dominate. With no information as to the magnitude of the secondary terms, except that they are much less than the main flow terms, many possibilities are available. As these parameters are individually allowed to approach limits, the equations (and hence the solutions) vary. For example, the governing equations change with increasing magnitude of  $p_0/P_0$  from the Schrödinger equation to the Boussinesq approximation for the secondary flow equations, to a general set containing all perturbation pressure related terms.

This procedure applied to (5) results in the following set of approximate equations describing the secondary flow. In addition to neglecting the higher order mo-

mentum transport terms, the effects of viscosity and the Coriolis force on the secondary flow are estimated to be at least an order of magnitude smaller than the remaining terms. This produces the simplest set of equations admitting secondary flow solutions. Henceforth, bars will be omitted from the mean velocity and pressure. Thus, we have

$$\left. \begin{aligned} Vu_y - Uz\psi_y &= 0 \\ V\psi_{zu} - Vz\psi_y + p_y/\bar{\rho} &= 0 \\ V\psi_{yu} + gT/\bar{T} + p_z/\bar{\rho} &= 0 \\ VT_u + \psi_z\bar{T}_u - \psi_y(\bar{T}_z + g/c_p) &= 0 \\ \rho/\bar{\rho} &= -T/\bar{T} \end{aligned} \right\}, \quad (6)$$

where  $v = \psi_z$ ,  $w = -\psi_y$ .

The validity of the above assumptions can be justified physically by the following arguments: compressibility effects are small within the planetary boundary layer and the Boussinesq approximation is applicable; and Coriolis forces are small in comparison to the other forces for flow at the secondary flow scale. Viscous effects generally cannot be neglected in the boundary layer. However, in the analysis of the Ekman/geostrophic boundary layer solution, the equations were made independent of  $Re$  (or  $\delta$ ) through an affine transformation so that viscous effects entered only in the vertical scaling, but not in the functional shape of the velocity profiles. Thus, one might expect "inviscid" instabilities, dependent only upon the shape of  $V/V_0$ , to still be retained in the frictionless equations. However, other "viscous" instabilities may be lost in this singular perturbation. Since the problem considered in this paper is the mesoscale, fully developed equilibrium flow at atmospheric Reynolds numbers in the range 500–4000, low-Reynolds-number "viscous" effects can be neglected.

For a horizontally homogeneous temperature field, there are three simultaneous equations in  $U$ ,  $V$ , and  $\psi$ , since  $u = (U_z/V)\psi$  and  $T = S\bar{T}\psi/V$  are obtained by direct integration from (6). The perturbation quantities can then be expressed in terms of the streamfunction and substituted into (2). These equations have been nondimensionalized using  $V_0$ ,  $\delta$  and  $\Delta\bar{T}$ , so that we have

$$\left. \begin{aligned} V\nabla^2\psi_y - (V_{zz} + gS/V)\psi_y &= 0 \\ 2V + U_{zz} - Re(U/V)_z\bar{\psi}_y &= 0 \\ 2U - V_{zz} - Re(\bar{\psi}_y\psi_{zz} - \bar{\psi}_z\psi_{yy} - P_y/\bar{\rho}) &= 0 \end{aligned} \right\}, \quad (7)$$

where  $\bar{T}$ ,  $P$  and  $\bar{\rho}$  are given;  $S = (1/\bar{T})(\bar{T}_z + g/c_p)$ ; and  $Re = V_0\delta/K_m = 2V_0/(\delta f)$ .

Eqs. (6), with  $V = 0$  (Couette flow,  $U_z$  constant), have been used by Kuo (1963) in a stability analysis. The nonlinear equations with  $U = V = 0$  and  $\bar{T}(z)$  have

also been discussed with latent heat release considered by Kuo (1961, 1965).

A numerical treatment of the complete Navier-Stokes equations has been done by Faller and Kaylor (1966), and steady-state finite perturbation rolls were obtained. The constant density case was used, no thermal effects were considered, and difficulties associated with stability and convergence inherent in the time-dependent integration of the entire equations limited the results to a few cases and Reynolds numbers  $< 500$ . Thus, this investigation [and Lilly's (1966)] was used to establish a critical Reynolds number of  $\sim 100$  for the onset of instability. This correlated well with observed rolls in Faller's dishpan experiments. However, atmospheric Reynolds numbers are an order of magnitude larger than this value. More recently, Faller and Kaylor<sup>2</sup> have included thermal effects, with, however, the same limitations with regard to Reynolds number and large computational times for equilibrium cases. A "quasi-equilibrium" state was obtained at  $Re = 900$ ,  $\epsilon = 10^\circ$ ; the results from this paper are in agreement for this case.

#### d. The energy balance

Eqs. (7) constitute a complete set of three equations in the three unknowns  $U$ ,  $V$  and  $\psi$ , with  $P$ ,  $\bar{\rho}$ ,  $S$  and  $Re$  given. Since the secondary flow equation is homogeneous in  $\psi$ , no magnitude can be obtained from the set, and  $U$  and  $V$  are solved for with respect to a normalized  $\psi/\psi_{max}$ . The maximum magnitude of the secondary flow can be obtained by considering the equilibrium energy balance.

As the secondary flow draws energy from the mean flow through the instability in the mean flow, it increases in magnitude until the mean momentum transport terms are sufficient to alter the mean profile. At this point, either the altered profile is more unstable, and energy is fed to the disturbance, leading to the breakdown of organized flow at this scale, or the profile becomes more stable. In the latter case, a steady state may be attained when the energy transferred is either only sufficient to balance secondary flow dissipation, or where it is zero, in the case where secondary flow dissipation is negligible.

From the momentum equations (6), an expression for the kinetic energy of the secondary flow is obtained, i.e.,

$$\frac{1}{2}(\partial/\partial t + V\partial/\partial y)(u^2 + v^2 + w^2) + uvU_z + vwV_z - \frac{wTg}{\bar{T}} + \frac{(w p_z + v p_y)}{\bar{\rho}} = 0. \quad (8)$$

This equation is integrated over the height of the

<sup>2</sup>Faller, A. J., and R. E. Kaylor, 1969: The generation of internal waves by shear flow instability. Presented at Amer. Geophys. Union Meeting, April, Washington, D. C.

boundary layer and a large lateral distance compared to this height in order to obtain the mean values

$$\begin{aligned} \partial E_2 / \partial t &= \int_0^H \int_0^L \underbrace{\partial / \partial t (q^2 / 2)}_{\text{change in secondary flow energy}} dy dz \\ &= \int_0^H \int_0^L \left[ \underbrace{-(uvU_z + vwV_z)}_{\text{interchange with the mean flow}} \right. \\ &\quad \left. + \underbrace{wTg/\bar{T}}_{\text{buoyancy effect}} + \underbrace{-(vp_y + wp_z)/\bar{\rho}}_{\text{secondary pressure work}} \right] dy dz. \end{aligned} \quad (9)$$

Considering a horizontally homogeneous mean flow, substituting the streamfunction, and performing the  $y$  integration, leaves

$$\left. \begin{aligned} v = \psi_z, \quad w = -\psi_y, \quad u = (U_z/V)\psi, \\ T = [(\bar{T} + g/c_p)/V]\psi \\ \partial E_2 / \partial t = \int_0^H [V_z \psi_z \psi_y + (U_z^2/V) \psi \psi_y \\ - g/(\bar{T}V)(\bar{T} + g/c_p) \psi \psi_y] dz \end{aligned} \right\} \quad (10)$$

The mean secondary flow pressure work is negligible consistent with the Boussinesq and perturbation approximations.

For a harmonic wave disturbance,  $\overline{\psi \psi_y} = 0$  (see Section 3), leaving

$$\int_0^H V_z \overline{\psi \psi_z} dz = \int_0^H V A dz = 0 \quad (11)$$

to be satisfied at equilibrium, where  $A(z)$  is the shape parameter obtained from the stability analysis in the next section.

Eq. (11) can also be obtained from (7) with neglect of secondary flow dissipation only. When (11) is written in dimensional, non-normalized form, the steady-state Landau equation for the perturbation magnitude results, i.e.,  $K_1 |\psi|^2 + K_2 |\psi|^4 = 0$ , where

$$K_1 = \int_0^H V_E A dz \quad \text{and} \quad K_2 = \int_0^H \bar{v} A dz,$$

$V_E$  is the Ekman profile and  $\bar{v}$  the mean modification due to the finite perturbations. This allows calculation of the secondary flow magnitude.

### 3. Solving the equations

#### a. The stability equations

Since the shape of the finite perturbations is assumed to be that of the most unstable (maximum growth rate) infinitesimal perturbation, a basic stability analysis is

needed. This is done by considering the time-dependent version of (5) less the perturbation product terms, defining a streamfunction for the nondivergent velocity field  $(v, w)$ , and assuming a periodic disturbance in time and lateral direction. The equations obtained are then:

$$\left. \begin{aligned} (V-c)(\Phi'' - \alpha^2 \Phi) - V_{zz} \Phi - g(\tau/T)_y - (1/i\alpha)(\rho\mu)' \\ = (1/i\alpha \text{Re})(\Phi'''' - 2\alpha^2 \Phi'' + \alpha^4 \Phi) \\ (V-c)\mu - U_z \Phi - \Phi'/(i\alpha) = (1/i\alpha \text{Re})(\mu'' - \alpha^2 \mu) \\ (V-c)\tau - (\bar{T}_y/i\alpha)\Phi' + (\bar{T}_z + g/c_p)\Phi \\ = (\text{Pr}/i\alpha \text{Re})(\tau'' - \alpha^2 \tau) \end{aligned} \right\} \quad (12)$$

where  $\psi = \Phi(z) \exp[i\alpha(y-ct)]$ ,  $T = \tau(z) \exp[i\alpha(y-ct)]$ ,  $u = \mu(z) \exp[i\alpha(y-ct)]$ , and  $\text{Pr} \equiv K_m/K_4$ .

In (12), the coupling of  $\Phi$  with the  $u$  velocity component is generally weak, being important only for large Coriolis force and small  $\text{Re}$ . When density-temperature perturbations are assumed negligible, then the equations reduce to those solved by Lilly (1966). His results substantiate the conclusions reached in the scale analysis that at typical atmospheric boundary Reynolds numbers, the Coriolis effect is negligible in determining maximum growth rates. These are determined by the dynamic instability associated with the inflection point in the  $V(z)$  profile. Barcion (1965) has discussed the conditions of large  $\alpha \text{Re}$  wherein the sixth-order stability equations including rotation can be approximated by the fourth-order Orr-Sommerfeld equation. Hence, for the neutral, horizontally homogeneous atmosphere, the equation for the perturbation is the Orr-Sommerfeld equation with the lateral mean velocity component as the governing parameter, i.e.,

$$\begin{aligned} (V-c)(\Phi'' - \alpha^2 \Phi) - V'' \Phi \\ = [1/(i\alpha \text{Re})][\Phi'''' - 2\alpha^2 \Phi'' + \alpha^4 \Phi]. \end{aligned} \quad (13)$$

This equation has received extensive analysis (Schlichting, 1960). Solutions indicate exponentially growing perturbations when  $V'' = 0$  somewhere in the velocity profile. This is an "inviscid" instability, obtainable from the "frictionless" Orr-Sommerfeld equation [the right side of (13) = 0], and remains valid despite the singular perturbation nature of this approximation.

Although the scale analysis indicates that the frictionless stability equation would be adequate to determine the needed shape functions, a computer program for solving the complete Orr-Sommerfeld equation for rather arbitrary  $V(z)$  was available, and was adapted to this particular problem. This provided another check on the validity of the assertion that the secondary flow is independent of viscous effects.

Under the assumption that the finite perturbations have essentially the same shape as the instability waves, the eigenfunctions for (13) have been obtained to use in solving (7) and (11). The solutions are given as normalized perturbations with respect to some maximum value of the finite perturbation. The form of the solution is given by magnitude  $|\Phi|$  and phase angle  $\phi$ , as a func-

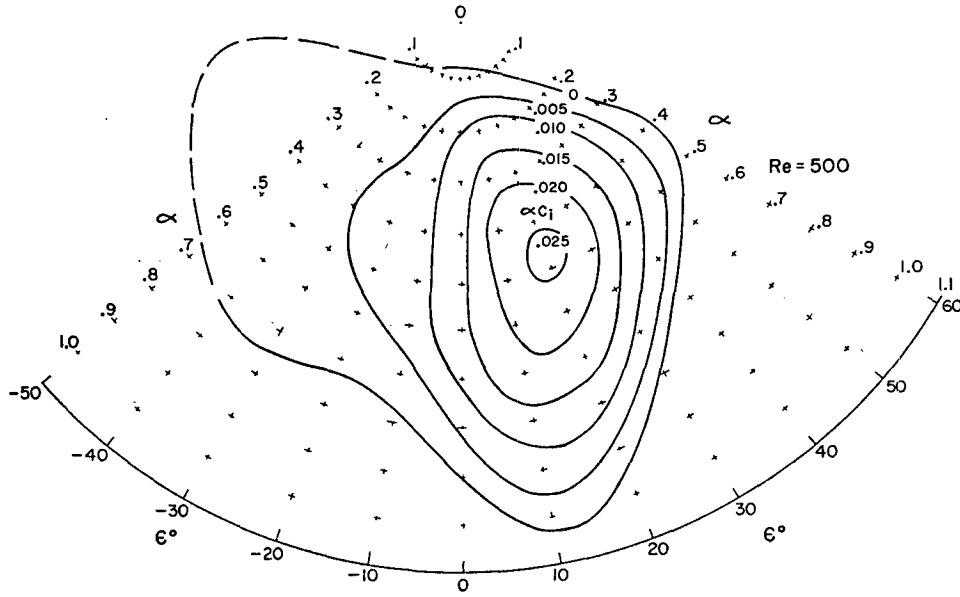


FIG. 2. Growth rates  $\alpha c_i$  vs orientation angle  $\epsilon$  and wavenumber  $\alpha$  for the unstable mode solution to the Orr-Sommerfeld equation. The Ekman mean flow is unstable inside the  $\alpha c_i = 0$  curve for the given  $Re = V_0 \delta / K_m$ . Units of  $\alpha c_i$  are  $V_0 / \delta$ , those of  $\alpha$  are  $1 / \delta$ .

tion of  $z$ , where  $\Phi = |\Phi| e^{i p}$  for a specific complex eigenvalue,  $c = c_r + i c_i$ . Here,  $c_r$  is the real wave speed, generally in the neighborhood of the  $V$  velocity near the inflection point value, and  $c_i$  is a measure of the growth rate,  $\alpha c_i$ , for this wave eigenfunction. The eigenvalue must be searched for, depending weakly upon the Reynolds number, the wavelength of the disturbance ( $\lambda = 2\pi/\alpha$ ), and the lateral velocity profile as represented by the angle  $\epsilon$  between the two-dimensional waves and the geostrophic velocity. Once the eigenvalue is found, the magnitude and phase of the associated complex eigenfunction is calculated.

The mean momentum transport terms can now be expressed in terms of  $\Phi$  and  $p$ , with  $\psi = |\Phi| e^{i p} e^{i \alpha y}$  (at equilibrium,  $c_i = 0$ ). However, this travelling wave has zero mean momentum transport. Energy transfer does take place, when a standing wave is considered, by adding a similar wave travelling in the opposite direction,  $\psi = |\Phi| e^{i \alpha y} + |\tilde{\Phi}| e^{-i \alpha y}$ , where  $\tilde{\Phi}$  is a complex conjugate. Upon substitution, expansion in  $\Phi = \Phi_r + i \Phi_i = |\Phi| (\cos p + i \sin p)$ , we have

$$\left. \begin{aligned} \overline{\psi \psi_y} &= 0 \\ \overline{\psi_z \psi_{zy}} &= 0 \\ \overline{\psi_y \psi_{zz}} &= 2\alpha (p' \Phi^2)' \end{aligned} \right\}$$

where the prime denotes  $d/dz$ .

The final set of working equations for determining the form and magnitude of the secondary flow and the modified mean flow can then be written, where the shape function is defined as  $A(z) = 2\alpha (p' \Phi^2)'$  and is obtained

from the solution to (13). This function is directly proportional to the mean momentum transport term. The mean flow is separated into a basic Ekman solution part plus a mean modification due to the finite perturbation components,  $\mathbf{V} = \mathbf{V}_E + \bar{\mathbf{v}}$ . A neutral atmosphere is assumed for the following solution. When the normalizing factor is reintroduced, the equations are as follows:

*Energy balance*

$$|\Phi|^2_{\max} = \int_0^H V_E A dz / \int_0^H \bar{v} A dz. \quad (14)$$

*Secondary flow solutions to (13)*

$$\left. \begin{aligned} v = \psi_z &= \alpha |\Phi(z)|' \\ &\times (\cos p \cos \alpha y - \sin p \sin \alpha y) |\Phi|_{\max} \\ w = -\psi_y &= \alpha |\Phi(z)| \\ &\times (\sin p \cos \alpha y + \cos p \sin \alpha y) |\Phi|_{\max} \end{aligned} \right\}. \quad (15)$$

*Mean flow modification from (7)*

$$\left. \begin{aligned} 2\bar{v} + \bar{u}_{zz} &= 0 \\ 2\bar{u} - \bar{v}_{zz} &= ReA \end{aligned} \right\}. \quad (16)$$

There are now five equations in the five unknowns,  $v, w, \bar{v}, \bar{u}$  and  $|\Phi|_{\max}$ .

*b. Solution for the mean flow modification*

Consider the mean flow modification equations (16), with

$$\bar{u}(0) = \bar{v}(0) = \bar{u}(z_{\max}) = \bar{v}(z_{\max}) = 0.$$

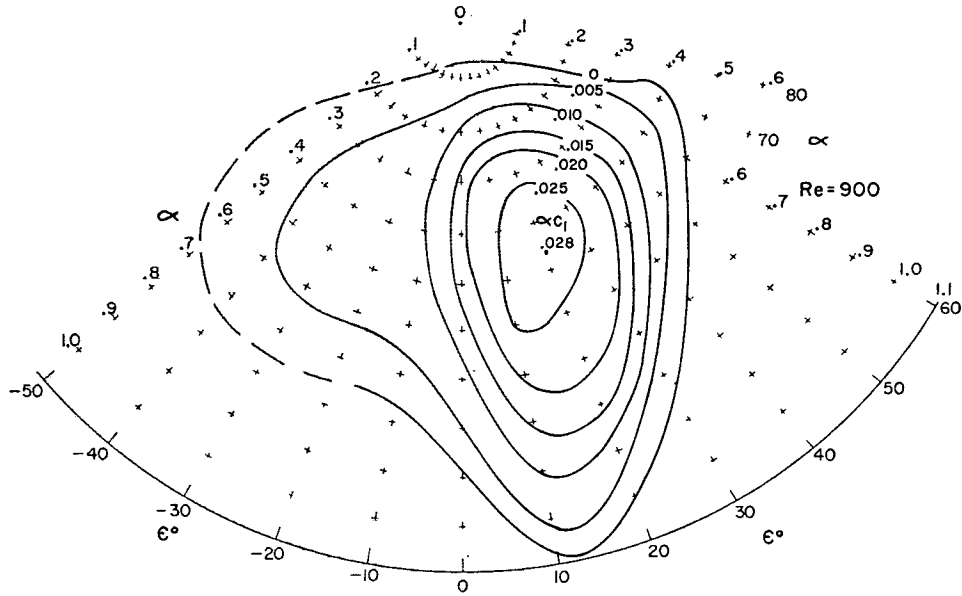


FIG. 3. Same as Fig. 2 except for Re=900.

The solution to this set is:

where

$$\left. \begin{aligned}
 \bar{v}(\zeta) &= C_1 \cosh \zeta \sin \zeta + C_2 \sinh \zeta \cos \zeta \\
 &\quad - \alpha \operatorname{Re} \int_0^\zeta \cosh(\zeta - \xi) \cos(\zeta - \xi) B(\xi) d\xi \\
 \bar{u}(\zeta) &= C_1 \sinh \zeta \cos \zeta - C_2 \cosh \zeta \sin \zeta \\
 &\quad + \alpha \operatorname{Re} \int_0^\zeta \sinh(\zeta - \xi) \sin(\zeta - \xi) B(\xi) d\xi
 \end{aligned} \right\} (17)$$

$$C_1 = \alpha \operatorname{Re} \int_0^{\zeta_m} [M \cosh \xi \cos \xi - N \sinh \xi \sin \xi] B(\xi) d\xi,$$

$$C_2 = \alpha \operatorname{Re} \int_0^{\zeta_m} [N \cosh \xi \cos \xi + M \sinh \xi \sin \xi] B(\xi) d\xi,$$

$$M = \cosh \zeta_m \sin \zeta_m / (\sinh^2 \zeta_m + \sin^2 \zeta_m),$$

$$N = \sinh \zeta_m \cos \zeta_m / (\sinh^2 \zeta_m + \sin^2 \zeta_m),$$

$$\xi \equiv \zeta_m - \xi,$$

$$B(\xi) \equiv p'(\xi) \Phi^2(\epsilon).$$

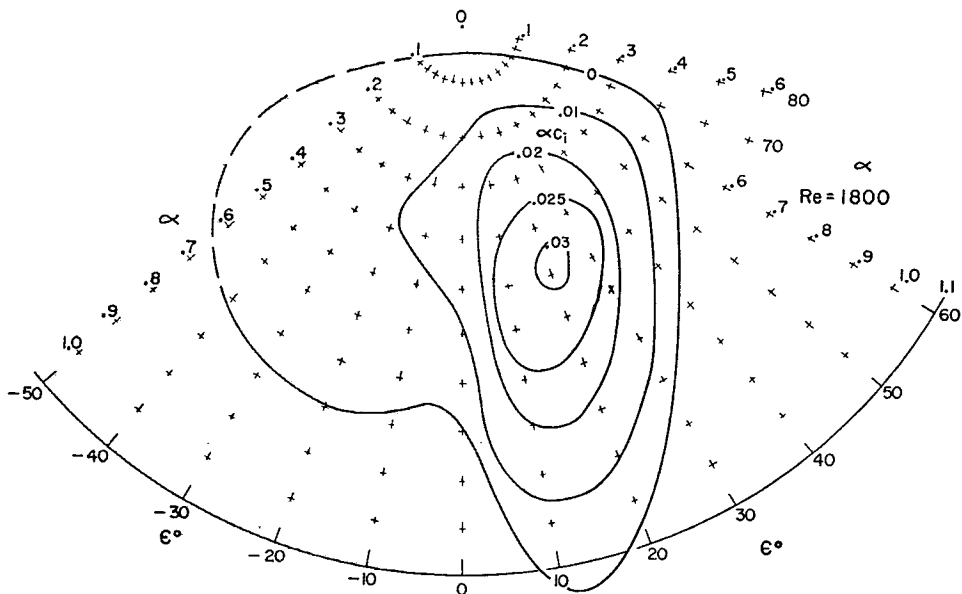


FIG. 4. Same as Fig. 2 except for Re=1800.

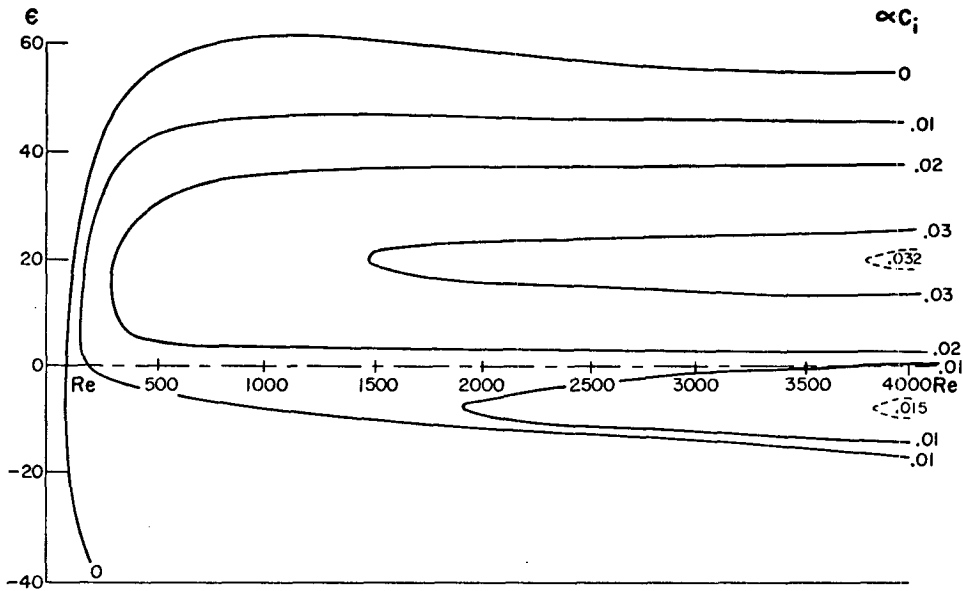


FIG. 5. Growth rates  $\alpha C_i$  vs orientation angle  $\epsilon$  and Reynolds number for  $\alpha = 0.5$ . The units are as in Fig. 2. Typical atmospheric Reynolds numbers are in the 500–4000 range.

There now exist sufficient equations for a solution to the problem. The Ekman velocities are obtained from (4); the shape parameter  $A(z)$ , the stream function normalized magnitude  $\Phi$  and phase  $p(z)$  are obtained from (13); the mean flow modification from (17); the normalizing factor  $|\Phi|_{\max}$  from (14); and finally, the perturbation velocities can be calculated from (15). The entire process has been programmed in Fortran IV.

Thus, the model results in a computerized concatenation which quickly and easily performs the following:

1) Calculates the general Ekman boundary layer profile for given synoptic variables plus a characteristic mean roughness parameter  $\delta$ . This parameter is Ekman's depth of frictional influence, or the  $e$ -folding length of the lateral velocity profile. It is proportional to  $K$ , the mean turbulent eddy viscosity.

2) Solves for the eigenvalues and eigenfunctions of the stability equation, the Orr-Sommerfeld equation.

3) Solves the set of equations for the equilibrium mean flow and the secondary flow magnitude and shape. As a check, the secondary dissipation term,  $u\nabla^2 u$ , is calculated.

4. Results

The basic result contained here is the boundary layer flow solution for a neutral atmosphere. It consists of a

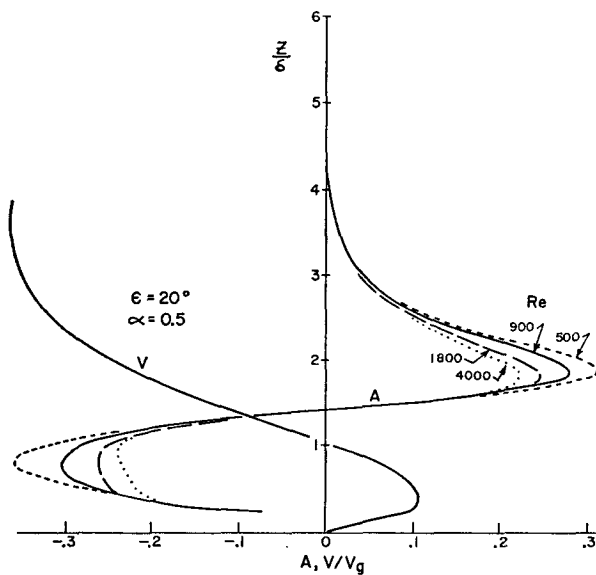


FIG. 6. The shape parameter, or mean momentum transport distribution,  $A$  (dimensionless) for the atmospheric range of  $Re$ , and the lateral Ekman velocity profile for the given  $\epsilon$  and  $\alpha$ .

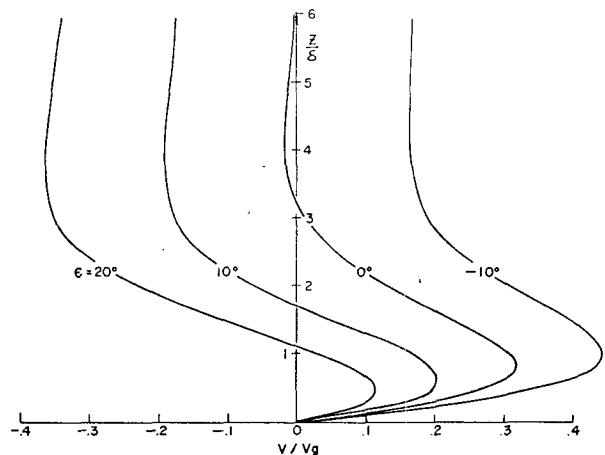


FIG. 7. Lateral Ekman velocity profiles at various orientation angles  $\epsilon$ .

modified Ekman boundary layer mean profile plus a secondary helical circulation. The external parameters determining the flow are the geostrophic wind, the latitude, and the local "roughness" as represented by an integrated mean  $K$  in the parameter  $\delta = (K/2f)^{1/2}$ . Several important internal parameters arise from the solution. They are  $\epsilon$ , the angle between the roll axis and the geostrophic flow at which the maximum growth rate occurs;  $A(z)$ , the shape factor which depends upon the eigenfunctions describing the phase and magnitude of the maximum growth instability waves; and  $|\Phi|_{\max}$ , the maximum magnitude of the secondary flow.

Figs. 2-4 are stability/growth rate plots as a function of  $\alpha$  and  $\epsilon$  for a given  $Re$ . From these graphs, critical  $\epsilon = 20^\circ$  and  $\alpha = 0.5$  are obtained. Although the growth rate values increase slowly with increasing  $Re$ , the critical values of  $\alpha$  and  $\epsilon$  are constant over the range of Reynolds numbers investigated. Partial surveys over  $\alpha$  and  $\epsilon$  at  $Re$  up to 4000 indicate nearly constant  $\alpha_{crit}$  and  $\epsilon_{crit}$ . When the stability curves for  $\epsilon$  vs  $Re$  at  $\alpha = 0.5$  are plotted in Fig. 5, the Reynolds number independence is apparent. This graph indicates that a secondary growth rate maximum region associated with the broad instability areas over negative  $\epsilon$  becomes more prominent at very high Reynolds numbers. This area represents a nearly parallel instability with  $\epsilon = -5^\circ$  for  $\alpha = 0.5$ . The significance of this high  $Re$  mode as  $Re \geq 5000$  requires further surveys such as those in Figs. 2-4 to

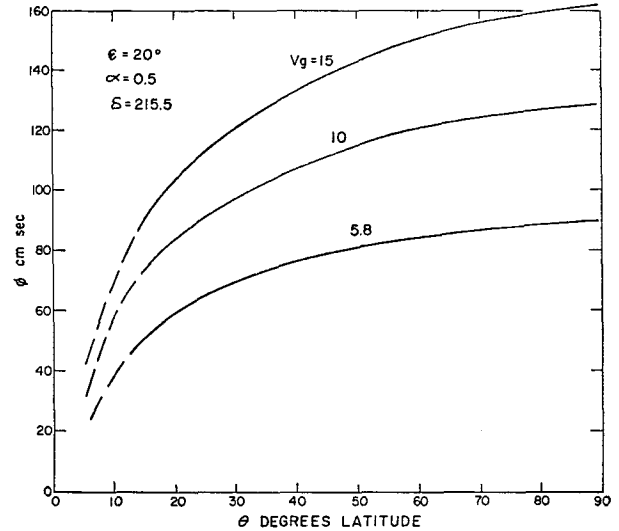


FIG. 9. Maximum secondary flow lateral velocities vs latitude  $\theta$ , for various  $V_g$  and given  $\epsilon$ ,  $\alpha$  and  $\delta$ .

determine whether  $\alpha_{crit}$  changes. Although these values of Reynolds number are greater than any considered in this paper, it is possible that they apply for very large  $V_g$ , smooth surfaces, and as the equator is approached. At the other end of the  $Re$  spectrum, the critical Reynolds number for neutral stability is  $\sim 100$ , in agreement with the values obtained by Fallor and Kaylor and by Lilly. There exists no clearly preferred  $\epsilon$  at this Reynolds number.

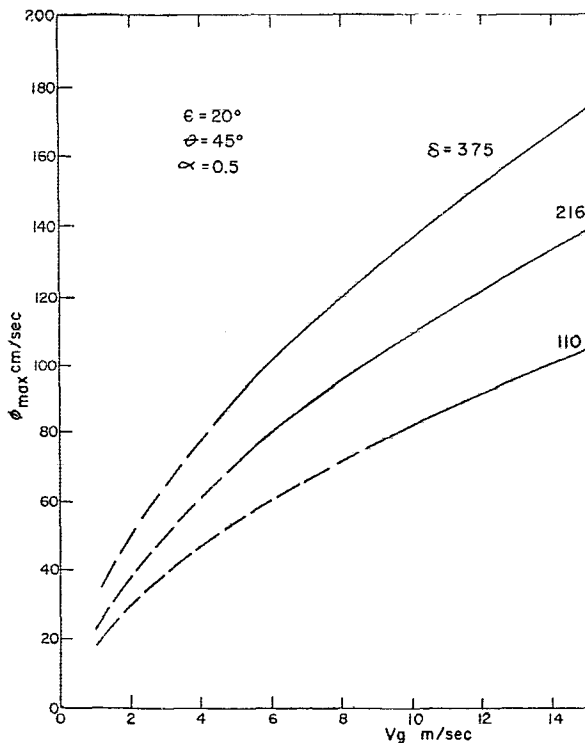


FIG. 8. Maximum secondary flow lateral velocities vs geostrophic velocity for various roughness parameters  $\delta$  and given orientation angle  $\epsilon$ , latitude  $\theta$ , and wavenumber  $\alpha$ .

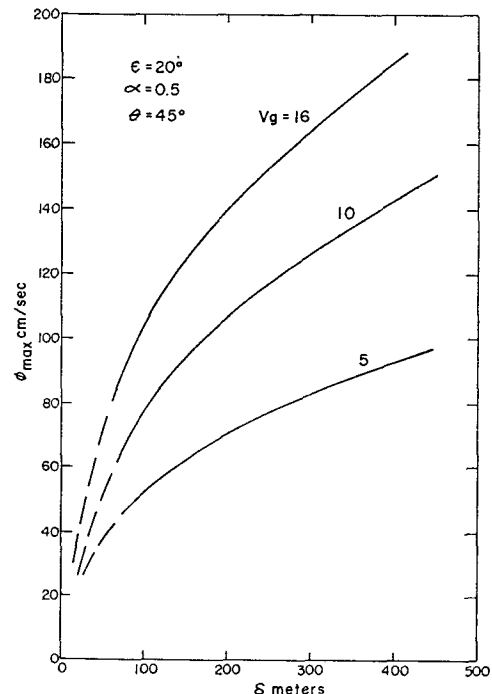


FIG. 10. Maximum secondary flow lateral velocities vs  $\delta$  for various  $V_g$  at given  $\epsilon$ ,  $\theta$  and  $\alpha$ .

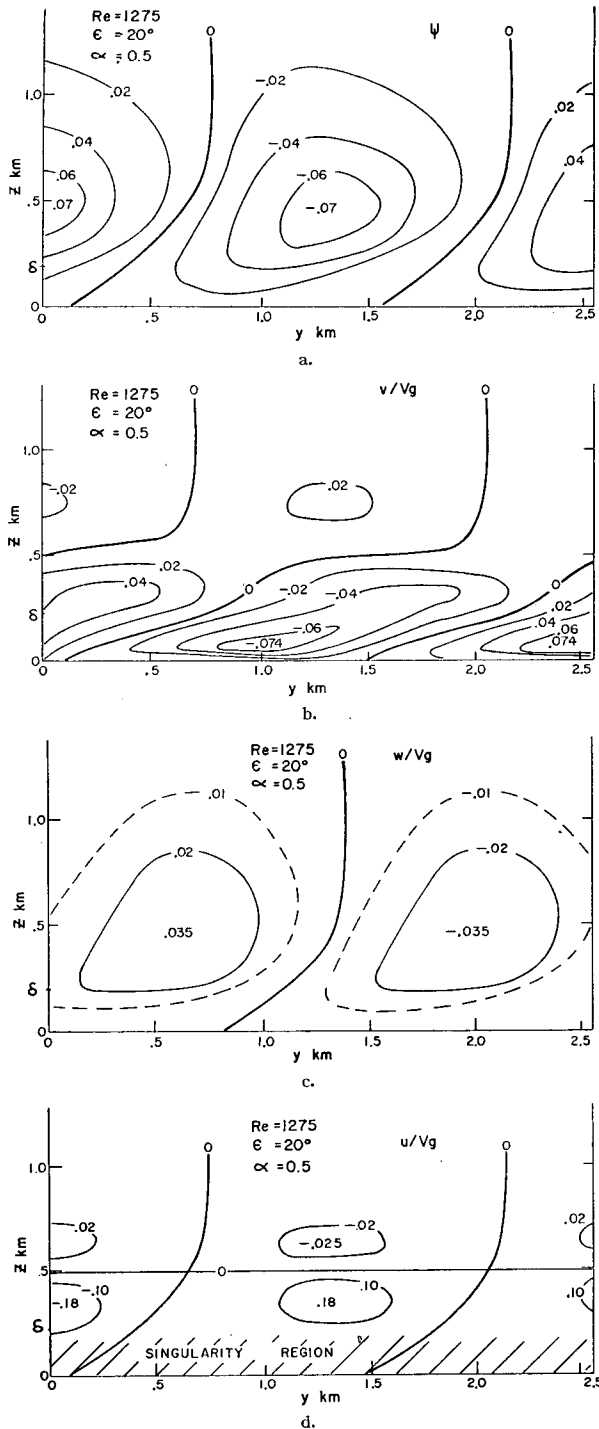


FIG. 11. Secondary flow patterns for case 2 (see Table 1),  $\theta=30^\circ$ ,  $\alpha=0.5$ ,  $\delta=215.5$  m,  $V_\theta=10$  m sec $^{-1}$ ,  $\epsilon=20^\circ$ ,  $Re=1275$ . The orientation angle and wavenumber correspond to maximum growth rate value. a. Secondary-flow stream function. These streamlines correspond to counter-rotating helices. The streamlines tilt in the direction of the mean wind shear. b. Secondary-flow lateral velocities. This represents the departure of the  $y$  component of flow from the mean value. c. Secondary-flow vertical velocities. d. Secondary flow longitudinal component. This component is decoupled from the lateral flow calculations and exhibits singular behavior unresolved by this calculation procedure. However, large values (18% of  $V_\theta$ ) are indicated.

The shape function  $A(z)$  is plotted in Fig. 6 for the critical  $\alpha$  and  $\epsilon$  and various  $Re$ . This term represents the mean momentum transport forcing function in the modified Ekman boundary layer equations, and occurs

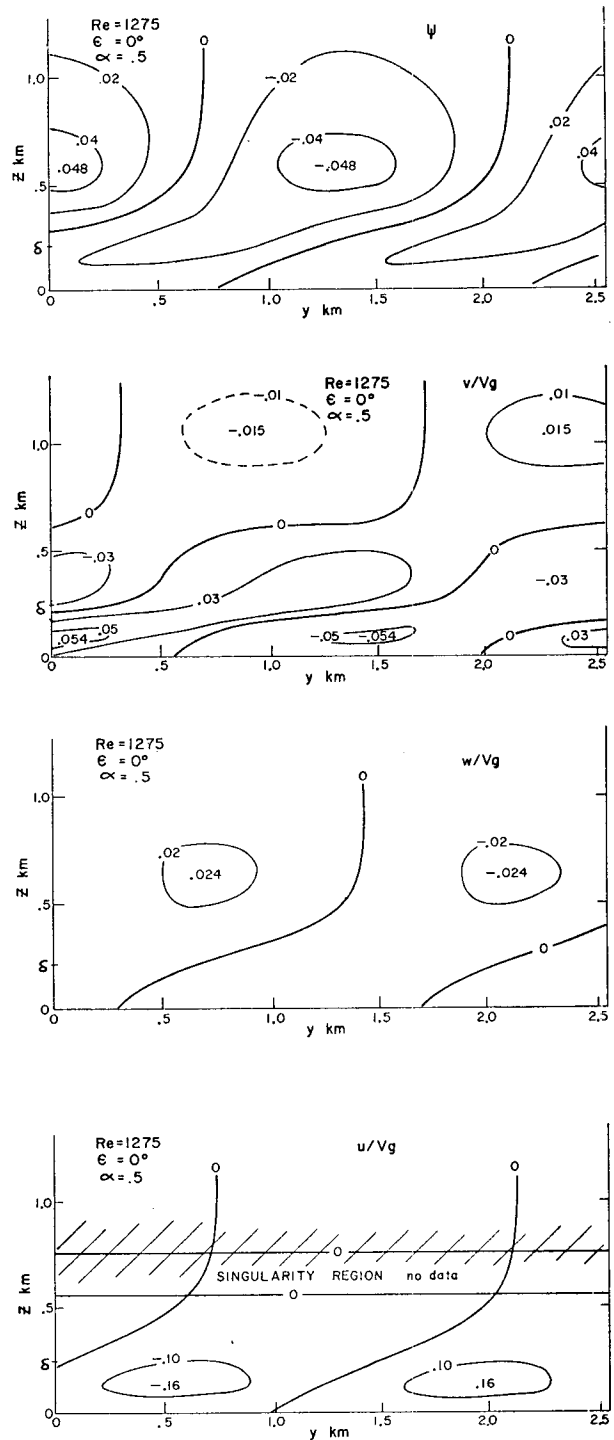


FIG. 12. Same as Fig. 11 except for case 5 (see Table 1)  $\theta=0$ . The orientation angle aligns the rolls with the geostrophic flow in this case.

TABLE 1. Secondary flow data for representative cases for the atmosphere.

Case	Latitude (deg)	Roughness (m)	$V_\theta$ (m sec <sup>-1</sup> )	Re	$\epsilon$ (deg)	$v_{max}$ (cm sec <sup>-1</sup> )	$w_{max}$ (cm sec <sup>-1</sup> )	$u_{max}$ (cm sec <sup>-1</sup> )	$H(\psi=0.02)$ (km)	$\lambda$ (km)
1	45	400	10	486	20	105	59	270	2.5	5
2	30	215.5	10	1275	20	73	35	180	1.1	2.7
3	45	110	10	1800	20	63	30	160	.55	1.38
4	30	110	16	4000	20	72	32	160	.44	1.38
5	30	215.5	10	1275	0	53	25	153	.55	2.7
6	45	215.5	5.6	500	20	58	32	151	1.34	2.7
7	45	215.5	13.3	1200	20	75	48	252	1.25	2.7
8	45	215.5	20	1800	20	126	60	320	1.04	2.7
9	15	215.5	10	2470	20	110	60	134	.97	2.7
10	80	215.5	10	650	20	94	50	250	1.27	2.7

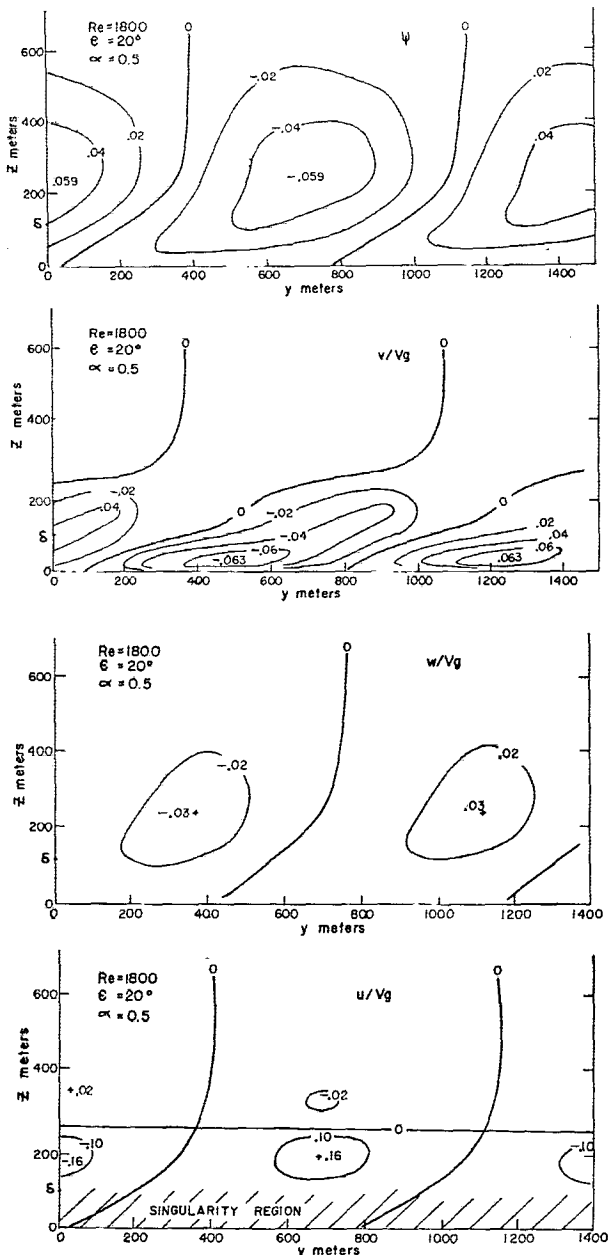


FIG. 13. Same as Fig. 11 except for case 3 (see Table 1)  $\theta=45^\circ$ ,  $\delta=110$  m,  $V_\theta=10$  m sec<sup>-1</sup>, Re=1800.

as a factor in the energy integral. It can be noted that in this maximum growth rate case, the product,  $-AV$ , is nearly maximized. This term is the kernel in the energy integral determining the energy available to the secondary flow. An increase in Reynolds number changes only the magnitude of this product.

Fig. 7 shows the shape of the Ekman lateral velocity profile for various  $\epsilon$ . These profiles possess an inflection point for all  $\epsilon$  with an increased velocity gradient across the inflection point as  $\epsilon$  increases. While there exist an infinite number of inflection points in the Ekman profile, the higher inflection points are associated with weak velocity gradients and can be expected to have weaker growth rates. Also, a full development of the Ekman profile in the atmosphere to include these detailed features is unlikely.

The behavior of the secondary flow magnitude as a function of the basic parameters of the flow,  $V_\theta$ ,  $\theta$  and  $\delta$ , is plotted in Figs. 8-10. The roughness parameter varies from a very smooth 110 to a rough 400. Faller (1965)

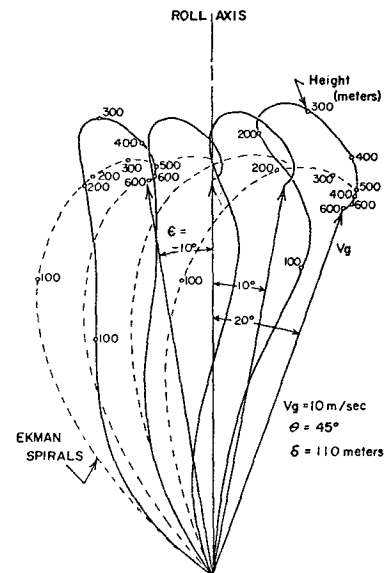


FIG. 14. Mean velocity hodographs for secondary flow model at given values of  $V_\theta$ ,  $\theta$  and  $\delta$  for  $\epsilon=-10, 0, 10$  and  $20^\circ$  and Re=1275. The height is indicated on the  $\epsilon=-10^\circ$  and  $20^\circ$  hodographs. All modified profiles exhibit increased alignment with the geostrophic direction and supergeostrophic velocities.

obtained the values  $\delta = 225$  for a smooth surface and 300 for a rough surface using an integrated  $K_m$  distribution obtained from the empirically derived profiles of Blackadar *et al.* (1965). These figures show that the secondary flow magnitude increases rapidly with increasing roughness or geostrophic velocity. The secondary flow maximum exhibits a sharp rise with latitude in the tropical regions, leveling off to a nearly constant value at the poles.

The cross-sectional values of  $\psi$ ,  $v$ ,  $w$  and  $u$  at typical stations are plotted in Figs. 11-13. The streamlines are similar for the entire range of  $Re$ ,  $\alpha$  and  $\epsilon$ . These figures show the flow shape to be almost independent of Reynolds number at the critical  $\alpha$  and  $\epsilon$ . While Fig. 12 shows the increased skewness of the phase for decreasing  $\epsilon$  corresponding to increased mean shear, the general roll shape is not very sensitive to changes in  $\epsilon$  over the unstable range. The extreme skewness of the lateral secondary velocity, with a maximum about 10% less than  $|\Phi|_{max}$ , and the circular symmetry of the vertical velocity profile, with maxima about 30% of  $|\Phi|_{max}$ , are also typical. A few representative cases with these maxima are given in Table 1. Since the  $u$  component is decoupled, the singular nature of this component did not interfere with the roll calculations. The singularities are of the removable type in the calculation of dissipation. However, accurate determination of  $u$  contours was generally not possible without an extensive refinement of the numerical procedures employed in the rest of the calculations. This limitation

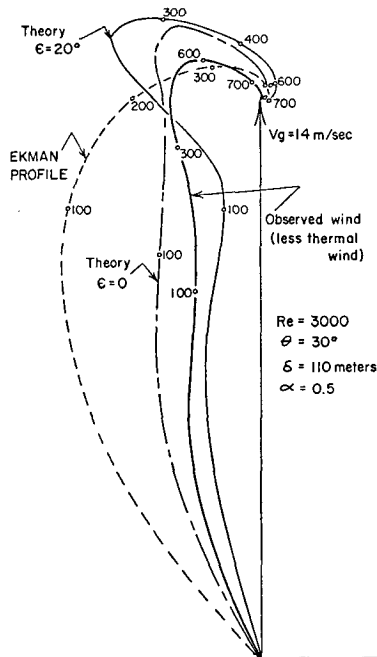


FIG. 15. Comparison of observed hodograph with modified mean hodographs at  $\epsilon = 0^\circ$  and  $20^\circ$  (the cloud streets of Fig. 1a indicate an orientation angle close to  $0^\circ$ ). The numbers give the height in meters.

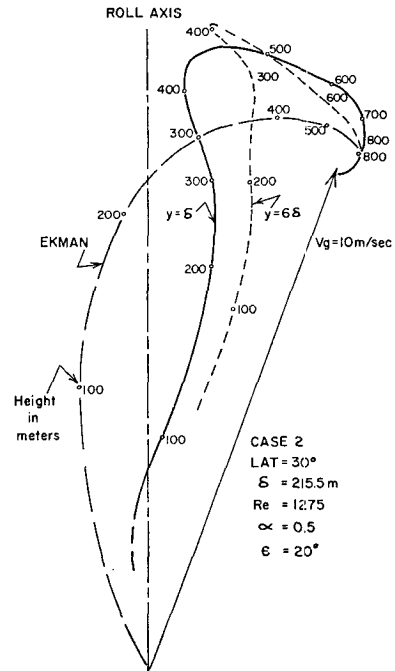


FIG. 16. Typical wind hodographs at lateral stations  $y = \delta$  and  $y = 6\delta$  for case 2 (Table 1). The lateral stations were chosen to indicate maximum secondary flow distortions to the mean profile. The hodographs show that large variations arise with respect to position in the rolls for an "instantaneous" profile.

makes  $u$  calculations for small  $z$  quite doubtful. Nevertheless, the rough values obtained are interesting in that fairly large values occur. Faller and Kaylor (1966) obtained a  $u$  component of 36%  $V_g$ . This component of the secondary flow results from vertical advection of the mean flow. Large values are confined to the lower region of the rolls corresponding to the region of large mean velocity gradient. The magnitudes of  $u$  at  $\epsilon = 20^\circ$  are approximately twice  $|\Phi|_{max}$ .

The modified mean profile at various  $\epsilon$  together with the unmodified Ekman profiles are plotted in Fig. 14 for a typical station. The extent of the modification is greatest at large positive  $\epsilon$  corresponding to the increased severity of the inflection point instability at these  $\epsilon$ . These profiles show the general characteristics of the secondary flow modification to the mean flow, an aligning of the flow in the geostrophic direction and the establishment of a low-level maximum velocity. The latter has been observed as a characteristic of Great Plains atmospheric boundary layer profiles, and is typical of trade wind latitudes (Blackadar, 1965, p. 10).

Fig. 1a is an Apollo photograph of the Georgia coast on 4 April 1968 with the accompanying meteorological data. The nearest wind velocity profile available was at Jacksonville,  $\sim 50$  miles south of the area of the photograph. However, conditions were very uniform over a wide area at this time. The inversion appears at least 400 km inland and 1000 km to sea. Using the temperature data from radiosonde profiles for Jacksonville,

Charleston and Montgomery, the thermal wind velocity component was calculated and subtracted out of the measured velocity profile in Fig. 1b. The horizontal temperature gradient is approximately uniform at  $1\text{C} (200\text{ km})^{-1}$ .

Fig. 15 compares this wind hodograph with the Ekman spiral and with two profiles calculated from the secondary flow model for the Jacksonville station at  $\epsilon=20^\circ$  (the maximum growth rate angle) and  $\epsilon=0$  (the estimated angle taken from the observations). A smooth value of  $\delta=110\text{ m}$  was used for this station, assuming that the vertical wind shear distribution was established over the ocean. This value of  $\delta$  corresponds to secondary flow magnitudes which essentially confine the rolls to the region under the observed inversion.

Finally, Fig. 16 shows the possible wind hodographs obtained at a fixed station in the lateral direction. These profiles are representative of those to be expected from an effectively instantaneous vertical profile within laterally moving rolls, or the profile at any station within stationary rolls. The two  $y$  stations were chosen to reflect maximum distortions to the basic wind profile, illustrating how the wind hodograph observed at a station is dependent upon its position relative to the rolls. A series of sample measurements taken at intervals would exhibit significant fluctuations about the mean profiles of Fig. 14 as the rolls were advected past.

## 5. Discussion

The object of this investigation was to develop a boundary layer model which would be applicable to large-scale areas; in particular, one which would give a rough estimate of the boundary layer-synoptic scale interaction, without regard to the inherent statistical nature of the normally turbulent boundary layer. Confidence in this approach was obtained by adducing from the growing body of evidence that there exist persistent, well-organized secondary flows embedded within the classical mean flows. Early observations consisted of isolated incidents such as Woodcock's (1942) observations of gull soaring habits, glider pilots' experience in long lifting bands (see Kuettner 1959), Langmuir's helical circulations in Lake George, and Kuettner's observations of the general band structure of the clouds. In the past five years, laboratory observations plus numerical integration of the time-dependent Navier-Stokes equations by Faller and Kaylor have presented additional evidence of the existence of vertical secondary flows in the boundary layer with rotation. Radar observations, tetron trajectories, satellite photos, and sometimes a good imagination, have indicated a fairly general existence of rolls several kilometers in lateral and vertical dimensions.

The simple Ekman boundary layer has not been observed as a regular geophysical boundary layer happening except in an isolated special case such as the oceanic boundary layer under an ice pack (Hunkins, 1969).

Although some indication of wind turning in the boundary layer is generally observed, the lack of a consistently shaped spiral as predicted by the Ekman theory, or even of a constant mean profile (see Zilitinkevich *et al.*, 1969) leads investigators naturally to the statistical domain of turbulence theory. This study has shown that highly variable profiles may be associated with the model developed here. The profile observed would depend upon the location of the observation within the rolls, the mean advection velocity of the rolls, and the orientation angle  $\epsilon$ —and hence the geostrophic flow direction, an ill-defined anchor. Nevertheless, a clear trend toward aligning the flow vector in the geostrophic direction is evident. A trend toward establishing a low level velocity maximum also is apparent. These are in general accordance with observations.

The analysis has indicated that the effect of viscosity appears only indirectly, by determining the shape of the mean profile. In particular, viscous dissipation in the secondary flow is negligible. Thus, equilibrium is defined as the point at which energy transfer is zero. As a check, the largest dissipation component was calculated using the equilibrium secondary flow velocities. It was found to be less than 10% of the energy supply corresponding to the unstable profile. If secondary flow dissipation was included, the energy consumed would result in a somewhat smaller modification to the unstable mean profile, to the point where the energy available due to the instability of the profile balances the dissipation.

The scale analysis showed the Coriolis forces to be small compared to the other forces in the secondary flow equations. This fact is critical to the further analysis, since it allows the decoupling of the lateral flow field from the  $u$  component and its attendant singularities. For the Ekman profile, the smallness of the Coriolis term is a result of using the "Ekman depth,"  $\delta=(2K_m/f)^{1/2}$ , as the characteristic length scale so that the Coriolis term parameter,  $f\delta/V_g=2/Re$ , vanishes in the "inviscid" limit of large  $Re$ . Similarly, the type II, or parallel (Lilly, 1966) instability mode is unimportant at typical atmospheric Reynolds numbers. Although the problem of the flow starting from rest must consider the lowest  $Re$  instability mode (Type II), it is assumed here that the Reynolds number increases so rapidly that low  $Re$  instability does not have time to develop, or that it does develop but becomes unimportant at higher  $Re$  (perhaps degenerating into small-scale turbulence). Another possibility is that stable stratification suppresses the instability so that the Ekman lateral profile can develop. If small-scale turbulence establishes an adiabatic layer under surface warming conditions, when the neutral layer reaches the inflection point depth (approximately  $=\delta$ ), Type I instability can be expected to operate.

The possibility that the constant disturbance shape assumption fails due to the altered mean profile as the disturbance grows is a more subtle criticism. The shape

of the perturbation depends upon the eigenvalue corresponding to maximum growth rate conditions and the resulting eigenfunction, which determines the vertical behavior of the secondary solution. The solution is determined by a particular combination of the phase  $\phi$  and amplitude of this eigenfunction. This combination is designated the shape function,  $A(z) \equiv 2\alpha(\phi'\Phi^2)'$ . It appears in the energy integral which determines the secondary amplitude, and as the forcing function, or nonlinear effect, in the modified mean flow equations. Except for a small magnitude change, the shape function is independent of Reynolds number variation. It is possible to derive, and solve in some instances, the second-order stability equations (Stuart, 1960; Watson, 1960; Perkeris and Shkoller, 1967). These results show that there is a small shift in the instability curves of Fig. 5 for the second-order equations. The attitude taken here is that once instability sets in, the first order maximum growth rate determines the most rapidly growing wavelength together with the corresponding critical eigenvalue. Since all wavelengths in the neighborhood of this critical wavelength are also unstable, a small shift in the stability curves is unlikely to change the finite, growing, initial instability wave significantly. Furthermore, the shape function is found to be insensitive to small shifts in the instability mode.

Evidence to this contention is found in the Faller and Kaylor (1966) time-dependent integrations of the entire equations, arriving at critical modes consistent with the first-order predicted modes. Also, the same shape assumption successfully predicted the observed wavelength in Charney's (1958) zonal flow model, and the Taylor-Görtler wavelengths in Stuart's analysis (1958).

At this point, the results can be used to speculate on their relation to some atmospheric phenomenon. From the behavior of the secondary flow magnitude vs latitude shown in Fig. 9, the rolls can be expected to appear from the poles to the tropics, but not at the equator, where the Ekman boundary layer itself is undefined. This agrees with observations—from Kuettner's, off the arctic tundra to Plank's over the Florida peninsula—and the absence of any observations indicating rolls at the equator.

The abrupt appearance of the cloud streets in direct conformity with the incidence of the geostrophic wind upon the coast in Fig. 1a may be explained by the behavior of secondary flow magnitude vs roughness. The incidence of land would imply an increase in roughness, of  $\delta$ , and consequently a jump in secondary flow magnitude. From Fig. 10 an increase in  $\delta$  implies an increase in secondary flow magnitude and the stronger circulation would raise the effective height of the rolls. This effect alone may be sufficient to produce clouds in incipient conditions. From the photograph in Fig. 1a, there exists a half-hour delay time in cloud formation, which requires a  $w(z)$  of about  $2 \text{ km hr}^{-1}$  or  $5\% V_g$ , typical values from this model.

The rolls imply a completely mixed layer of about one-half wavelength depth. Critical wavelengths obtained in this analysis were about  $\lambda = 12\delta$ . This corresponds to roll heights of about 1–3 km for  $\delta = 100$ –400 m. Due to surface layer heating and subsequent mixing, an adiabatic layer would be rapidly established, tending to create inversions above the adiabatic layer. Although a paucity of data on inversion behavior inhibits checking this hypothesis, there exist some indications that the secondary flow and the inversion are linked. Langmuir's measurements indicated a correspondence between the rolls and thermoclines. Such secondary circulations offer a possible explanation for these otherwise difficult to explain phenomena such as the multiplicity of sharp, persistent thermoclines (Woods, 1968; Langmuir, 1938).

The method of obtaining eigenvalue solutions to the Orr-Sommerfeld equation does not facilitate investigating new eigenvalue modes. Each mode requires graphical interpolations to establish sufficiently accurate eigenvalues so that convergence is obtained within the program. Once such an eigenvalue is found, the stability over  $\text{Re}$ ,  $\alpha$  and  $\epsilon$  can be explored by slowly varying each parameter, a computer time-consuming process. Nevertheless, the indications of a second, parallel instability region in Fig. 5 suggest that further exploration of the eigenvalue modes at high Reynolds numbers may be revealing. Atmospheric Reynolds numbers can reach 5000. However, secondary flow magnitudes for this region appear to be small, about  $2\% V_g$ .

Some method of establishing values for  $\delta$  is needed for this model if secondary flow magnitudes are to be determined. When  $\delta$  is determined by a mean  $K_m$ , the latter should correspond to the small-scale turbulence only, since the constant  $K_m$  used to obtain the basic Ekman profiles excludes secondary flows. Thus, the integrated mean  $K_m$  taken from empirical data such as Blackadar *et al.* (1965; see Faller, 1965) may include secondary flow fluxes and has been used only as an upper limit to establish the approximate range of  $\delta$  to be investigated. One may speculate that the secondary flow implies an altered momentum flux from that associated with a constant  $K_m$ , inferring a variable  $K_m(z)$  distribution appropriate to the stable mean profiles (Fig. 14).

The large values of the secondary  $u$  component suggest this term may prove interesting for further investigation. The approximations in this model are stretched to their fullest in the calculation of this term. This is evident in the rigid bounds of the  $u$  component in Figs. 11d–13d. The  $u$  component dissipation was only roughly calculated, and although it was generally less than  $10\%$  of the other energy terms, it should be included in a quantitatively more accurate treatment. This process would involve using more accurate derivative calculation methods, integrating methods, smaller grid sizes near singularities, and an iteration process in the energy balance.

Perhaps the most important direction for expanding the model capability is toward the inclusion of stratification, and ultimately consideration of the entire set of stability equations. Currently, solutions to the Orr-Sommerfeld equation modified to include the buoyancy term have been obtained for a Blasius velocity profile by Fang Lee. This modification is being incorporated into the present, finite perturbation program.

*Acknowledgments.* Prof. Robert Fleagle provided much to this paper with his suggestions, encouragement, salient criticism and ready availability for discussion throughout its development. Considerable constructive criticism, plus perceptive and valuable suggestions were contributed by Prof. J. Holton. Discussions with Profs. J. Businger, C. Leovy and J. Ching were also profitable. Particular thanks are due Dr. Fang Lee for the generous contribution of his basic program for solving the Orr-Sommerfeld equation and the helpful discussions on the modification for this problem.

Support during this work was obtained from the National Science Foundation under Grant GA-1099.

#### REFERENCES

- Angell, J. K., and D. H. Pack, 1967: Helical circulations in the planetary boundary layer. *Boundary Layer and Turbulence*, Amer. Inst. Phys., 226-229.
- , —, and C. R. Dickson, 1968: A Lagrangian study of helical circulations in the planetary boundary layer. *J. Atmos. Sci.*, **25**, 707-717.
- Barcilon, B., 1965: Stability of non-divergent Ekman layers. *Tellus*, **17**, 53-68.
- Blackadar, A. K., 1962: The vertical distribution of wind and turbulent exchange in a neutral atmosphere. *J. Geophys. Res.*, **67**, 3095-3102.
- *et al.*, 1965: Flux of heat and momentum in the planetary boundary layer of the atmosphere. Final Rept., AFCRL-65 631, Penn. State Univ.
- Charney, J., 1958: On the general circulation of the atmosphere. *The Rossby Memorial Volume*, New York, Rockefeller Institute Press, 178-193.
- Ekman, V. W., 1905: On the influence of the earth's rotation on ocean currents. *Arkiv. Math. Astron. Fysik.*, **2**, 1-54.
- Faller, A. J., 1965: Large eddies in the atmospheric boundary layer and their possible role in the formation of cloud rows. *J. Atmos. Sci.*, **22**, 176-184.
- , and R. E. Kaylor, 1966: A numerical study of the instability of the laminar Ekman boundary layer. *J. Atmos. Sci.*, **23**, 466-480.
- Hanna, S., 1969: The formation of longitudinal sand dunes by large helical eddies in the atmosphere. *J. Appl. Meteor.*, **8**, 874-883.
- Hicks, J., and J. K. Angell, 1968: Radar observations of breaking gravitational waves in the visual clear atmosphere. *J. Appl. Meteor.*, **7**, 114-121.
- Hunkins, 1969: Ekman drift currents in the Arctic Ocean. *Deep Sea Res.*, **13**, 607-620.
- Kuetner, J., 1959: The band structure of the atmosphere. *Tellus*, **11**, 267-294.
- , 1967: Cloudstreets, theory and observations. *Aero Revue*, **42**, 52-56, 109-112.
- Kuo, H., 1961: Convection in a conditionally unstable atmosphere. *Tellus*, **13**, 61-71.
- , 1963: Perturbations of plane couette flow—stratified fluid and original cloud streets. *Phys. Fluids*, **6**, 145-211.
- , 1965: Further studies of the properties of cellular convection in a conditionally unstable atmosphere. *Tellus*, **17**, 4-13.
- Langmuir, I., 1938: Surface motion of water induced by wind. *Science*, **87**, 119-123.
- Lilly, D. K., 1966: On the stability of Ekman boundary flow. *J. Atmos. Sci.*, **23**, 481-494.
- Malkus, J. S., and G. Veronis, 1958: Finite amplitude cellular convection. *J. Fluid Mech.*, **4**, 225-260.
- NASA, 1967: *Earth Photographs from Gemini III, IV, and V*. NASA SP-129, Gov't Printing Office.
- Pekeris, C., and B. Shkoller, 1967: Stability of plane Poiseuille flow to periodic disturbances of finite amplitude in the vicinity of the neutral curve. *J. Fluid Mech.*, **29**, 31-38.
- Plank, V., 1965: The cumulus and meteorological events of the Florida peninsula during a particular summertime period. Tech. Rept. AFCRL-65-761, Bedford, Mass.
- Roll, H., 1965: *Physics of the Marine Atmosphere*. Intern. Geophys. Series, Vol. 7, New York, Academic Press, 308 pp.
- Schlichting, H., 1960: *Boundary Layer Theory*. New York, McGraw-Hill, 647 pp.
- Stuart, J. T., 1958: On the non-linear mechanics of hydrodynamic stability. *J. Fluid Mech.*, **4**, 1-21.
- , 1960: On the non-linear mechanics of wave disturbances in stable and unstable parallel flows, Part 1. *J. Fluid Mech.*, **9**, 353-370.
- Watson, J., 1960: On the non-linear mechanics of wave disturbances in stable and unstable parallel flows, Part 2. *J. Fluid Mech.*, **9**, 371-380.
- Woodcock, A. H., 1942: Soaring over the open sea. *Sci. Monthly*, **55**, 226-232.
- Woods, J., 1968: Wave induced shear instability in the summer thermocline. *J. Fluid Mech.*, **32**, 791-800.
- Zilitinkevich, Laikhtman and Monin, 1969: Dynamics of the atmospheric boundary layer. *Izv. Atmos. Oceanic Phys.*, **3**, 297-333.